JACS
JOURNAL OF THE AMERICAN CHEMICAL SOCIETY
pubs.acs.org/JACS
Article

Redox Staining of Metallic Lithium inside Batteries for Multimodal Visualization and Identification with Multiscale Spatial Resolution

Jun Ho Lee,[▽] Jane K. J. Lee,[▽] Pu Zhang, Sarah E. Holmes, Wenbo Zhang, Il Rok Choi, Sang Cheol Kim, Junyoung Lee, Sanzeeda Baig Shuchi, Mun Sek Kim, Zhenan Bao, Wah Chiu,* and Yi Cui*

Cite This: J. Am. Chem. Soc. 2026, 148, 30019−30028
Read Online
ACCESS | Metrics & More | Article Recommendations | Supporting Information

ABSTRACT: The dynamic behaviors of metallic lithium (Li^0) in Li-based batteries including the formation of various morphologies, corrosion, isolation, and spatial distribution affect the cycle life and safety. However, analysis on formation mechanisms or governing factors of Li^0 is largely limited by the lack of experimental techniques to chemically and spatially identify low-Z elements from nano- to macroscale. Here, we demonstrate that staining Li^0 with high-Z elements via redox reactions effectively enhances its visibility under an electron beam or X-rays. We find that heavy metal ions (M^{n+}) can be reduced by Li^0 and nucleate as nanoparticles (NPs) on surfaces, staining effectively for direct visualization. Our results demonstrate that inactive Li^0 embedded within residual SEI can be visualized, thereby revealing correlations between its distribution and its electrochemical performance such as Coulombic efficiency (CE). Our new technique represents a new analytical characterization tool to spatially track previously "invisible" internal components in batteries.

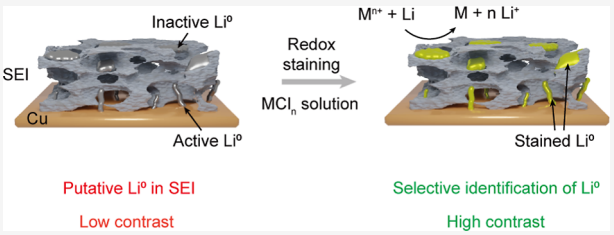

INTRODUCTION

Electrodeposition of Li^0 during cycling influences Li battery performance and raises safety concerns. Electrolyte decomposes to form the solid electrolyte interphase (SEI) due to the high reactivity of Li^0, and the dendritic morphology of Li^0 can induce short circuits inside Li batteries. Furthermore, repeated plating/stripping of dendritic Li^0 is responsible for the buildup of SEI and electrically isolated Li^0 (inactive Li^0) in Li-ion batteries (LIBs) and Li metal batteries (LMBs).[1−9] In particular, the accumulation of inactive Li^0 is reported to cause substantial capacity loss accompanied by corrosion in charged states. Recent efforts have been made to mitigate inactive Li^0, but fundamental understanding of its formation is limited.[10−12] For example, cycling factors such as pressure, current density, and the composition of the SEI might influence the size and spatial distribution of inactive Li^0. However, the correlation between them has not been studied.[13−15] Given that Li^0 plating produces features spanning from the nanoscale to the electrode scale, simultaneous analysis across different scales is essential. Thus, elucidating comprehensive aspects of Li^0 in multiscale is critical to understanding and improving battery performance.

Unfortunately, the lack of characterization tools to identify and visualize low-Z elements has limited the analysis of Li^0. Although scanning electron microscopy (SEM) can obtain morphological information on Li^0 at a charged state, low-energy characteristic X-ray hinders the utilization of energy-dispersive spectroscopy (EDS)[16−20] for characterization. The employment of cryogenic electron microscopy (cryo-EM) equipped with electron energy loss spectroscopy (EELS) has enabled simultaneous visualization and identification of Li^0, but typically at the nanoscale and challenging to detect Li^0 when surrounded by thick SEI.[21,22] On the other hand, titration gas chromatography (TGC) serves as an electrode-level quantification method for inactive Li^0. But it is limited by the lack of spatial resolution and its destructive nature.[2,23] Furthermore, identifying inactive Li^0 in the discharged state, embedded within the low-Z elements of the SEI matrix formed during cycling (residual SEI), has not been possible. It is challenging to correlate microscopic images to battery performance without simultaneous chemical and spatial resolution. Thus, developing a generalized technique that enables identification and visualization of Li^0 with multiscale spatial resolution is essential, and no such technique has been developed to date.

Staining is a widely used technique in biology to visualize individual cell components through labeling or tagging.[24−26] Features of interest can be selectively highlighted by enhanced contrast under various incident lights, including visible light and electron beams. The technique has transformed the field by enabling mechanistic studies of the spatial location of

Received: March 23, 2026
Revised: June 30, 2026
Accepted: July 1, 2026
Published: July 10, 2026

https://doi.org/10.1021/jacs.6c05427
J. Am. Chem. Soc. 2026, 148, 30019−30028

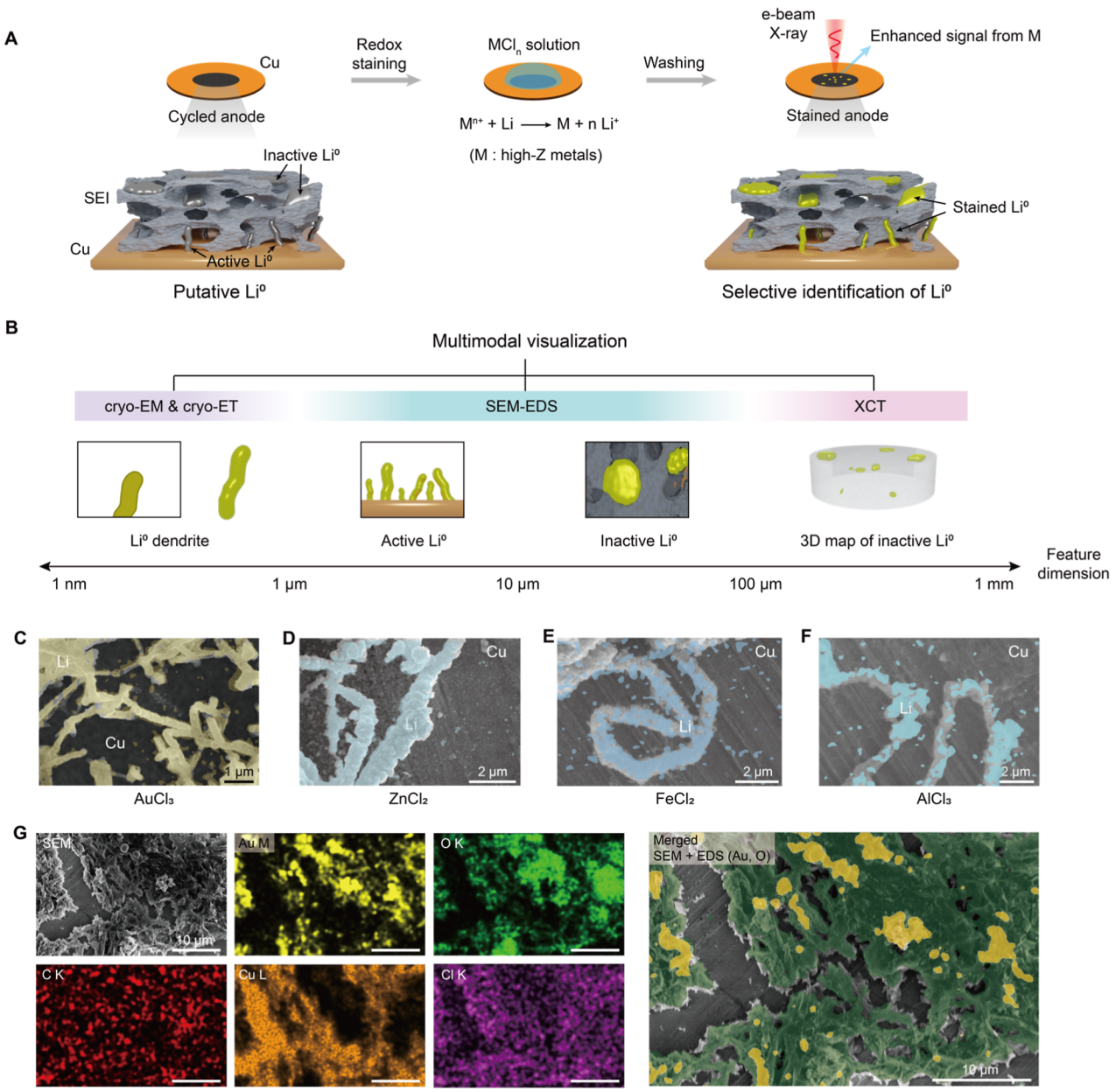

Figure 1. Multimodal visualization of Li^0 through redox staining. Schematic depicting the concept of Li staining in Li batteries inspired by biological cell staining. (A) Scheme displaying active and inactive Li^0 embedded within SEI (light gray) before (left) and after staining (right). The color of Li^0 species changed from dark gray to yellow during redox staining with MCl_n solution (M: high-Z element). (B) Illustration of Li^0 staining in multiscale visualization. Characterization techniques, their typical detection ranges of features, and corresponding schemes were visualized (high Z element, Li^0, residual SEI, and Cu are in yellow, light gray, dark gray, and orange, respectively). (C−F) Merged SEM-EDS images of Li dendrites plated at 1 mA cm^{-2} for 0.25 mAh cm^{-2}. Dendrites were stained with $AuCl_3$ (C), $ZnCl_2$ (D), $FeCl_2$ (E), and $AlCl_3$ (F), and binary EDS maps of Au M, Zn L, Fe K, and Al K, respectively, were depicted in corresponding images. (G) Representative SEM and corresponding EDS maps of residual SEI after the 1st cycle of charging and discharging (1 mA cm^{-2} for 0.5 mAh cm^{-2}), followed by Au staining. The merged image of SEM, EDS Au M map (yellow), and EDS O K map (green) is shown on the right. All cells were cycled with 1 M LiFSI in the DME electrolyte.

biological features. Inspired by this technique, we propose that the staining of low-Z elements with high-Z elements for batteries to enhance their detectability is feasible through redox reactions. Heavy metal precursors (M^{n+}) can stain the Li^0 surface through a reduction reaction, n Li^0 + M^{n+} → n Li^+ + M^0, enabling the Li^0 surface to stand out from the surrounding SEI (Figure 1A). Combined with characterization techniques, this method allows high chemical and spatial resolution of Li^0 at all battery length scales, resulting in comprehensive insights into the factors governing its formation (Figure 1B). Moreover, we expect the technique to be applied to broader scopes beyond LMBs and have a significant impact on the analysis of low-Z elements across many fields.

RESULTS AND DISCUSSION

Design Principles of Staining for Li^0

To enable selective redox staining for Li^0, three crucial criteria should be met. (i) The staining agent should consist of a high atomic number (Z) element, preferably higher than Mg. High-Z elements contribute to enhanced contrast due to a greater number of backscattered electrons under electron beam

https://doi.org/10.1021/jacs.6c05427
J. Am. Chem. Soc. 2026, 148, 30019−30028

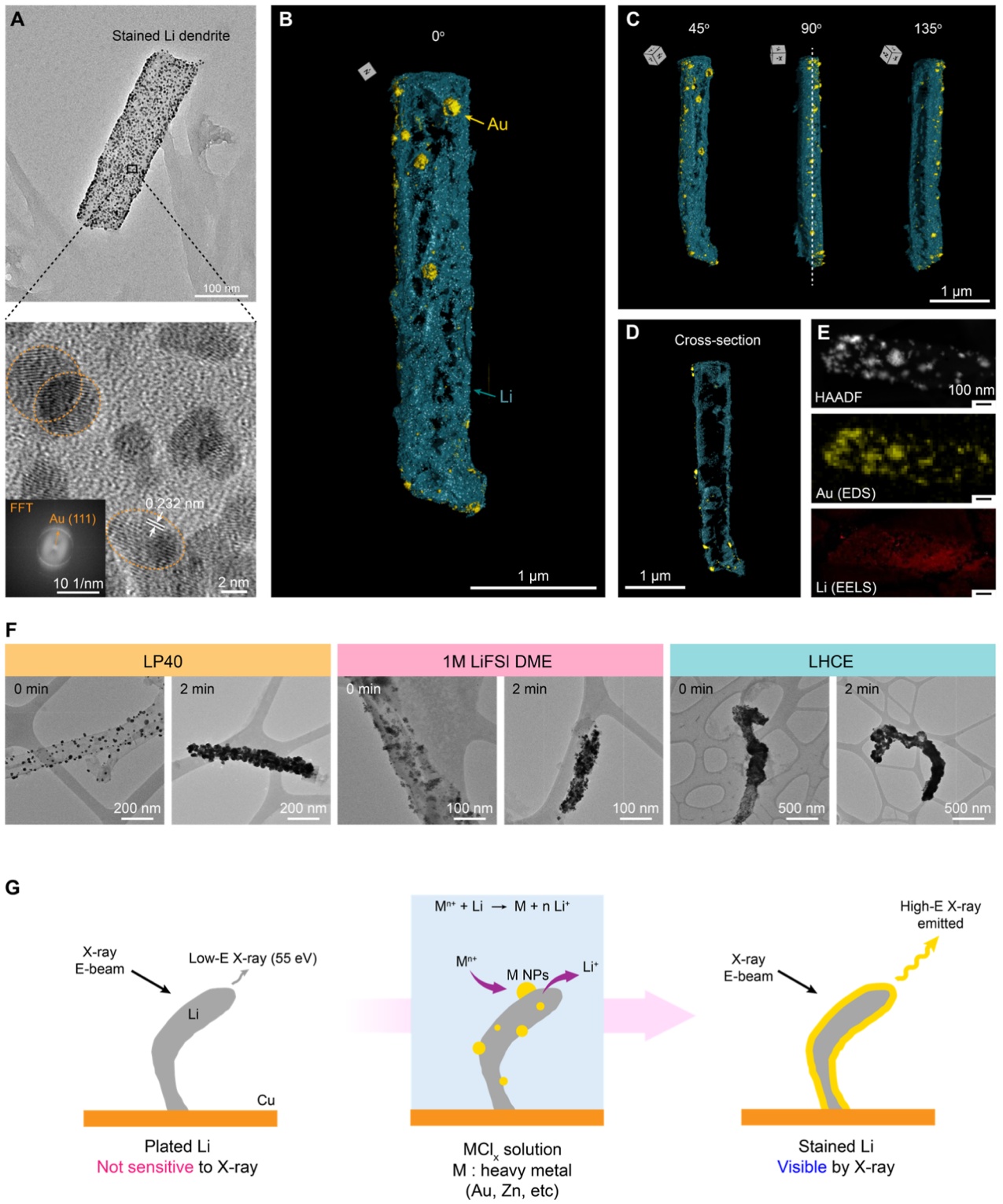

Figure 2. Cryo-EM study on the staining mechanism of Au. (A) Cryo-EM image of the Li^0 dendrite after Au staining with a zoom-in and higher-resolution image of a boxed region and its corresponding Fourier power spectrum. Orange dotted lines indicate NPs. (B–D) 3D-reconstructed image of the Au-stained (yellow) Li^0 dendrite (dark cyan) at 0° (B), 45°, 90°, and 135° (C). (D) The central cross-sectional image of the plane represented by the white dotted line in (C). (E) HAADF (top), Au EDS map (middle), and Li EELS map (bottom) of a stained dendrite. Scale bar, 100 nm. (F) Cryo-EM images of Li^0 dendrites ~ 0 and 2 min after the staining reaction in LP40 (orange), 1 M LiFSI in DME (pink), and LHCE electrolytes (cyan). (G) Scheme of the proposed mechanism of staining on Li dendrites.

irradiation and higher-energy characteristic X-rays. (ii) M^{n+} should have a higher electrochemical reduction potential than Li (−3.04 V vs standard hydrogen electrode (SHE)) to induce nucleation of M on the Li^0 surface. (iii) Nucleated particles should selectively deposit on Li^0 and remain spatially colocated during visualization. Detection of M^0 should simultaneously preserve the location and morphology of the Li^0 surface. Following this rationale, $AuCl_3$ in 1,2-dimethoxyethane

https://doi.org/10.1021/jacs.6c05427
J. Am. Chem. Soc. 2026, 148, 30019−30028

(DME) is chosen due to the high reduction potential of Au^{3+} ($Au^{3+} + 3\ e^- \rightarrow Au$; 1.52 V vs SHE) and broad utilization of Au particles for various characterizations.[27,28] We observed the surface color change after applying $AuCl_3$ solution to Li^0 foil and chose 0.05 M as the optimal concentration to minimize SEI dissolution (~5 min) without excessive precipitation (Figure S1A,B).[29] Similar experiments on pancake-like Li^0 confirmed selective staining through contrast enhancement of the Li^0 surface in SEM, along with strong Au M signals exhibiting matching morphology in EDS analysis (Figure S1C).[30]

Li dendrites in an ether electrolyte—0.25 mAh cm^{-2} plated in 1 M LiFSI in DME (1 M DME)—were used to verify chemical identification of redox staining at a battery-relevant scale. In Figure 1C, a binary image of the Au M EDS map displayed a strong correlation in terms of morphology and location with the surface of Li dendrites, indicating that the staining successfully preserves morphological and spatial information on Li^0 at the μm-scale. Selective deposition of Au with higher-energy characteristic X-ray (~2.123 keV) than Li^0 (~55 eV) enabled utilization of the Au M signal for chemical identification of Li^0. In contrast to Au M signals, the EDS maps of other elements did not show as strong a correlation with the corresponding SEM image (Figure S2A). Similar results with $ZnCl_2$, $FeCl_2$, and $AlCl_3$ precursors indicated that the staining could be coupled with other higher Z elements and not limited to Au (Figures 1C−F and S2B−D). Reduction potentials of Zn^{2+} (−0.76 V vs SHE), Fe^{2+} (−0.44 V vs SHE), and Al^{3+} (−1.66 V vs SHE) also suggested that they could participate in redox reactions with Li^0. Our results illustrated the feasibility of redox staining on Li^0 at the charged state under battery conditions.

To systematically understand the morphological changes from staining, we plated Li^0 onto Cu TEM grids and compared the thickness of Li^0 dendrites after staining with 10 mM, 50 mM, and 100 mM of $AuCl_3$ DME solution for 0.5, 1, and 2 min (Figure S3). Stained and unstained samples were prepared simultaneously from the same coin cell to minimize cell-to-cell variability. By collecting the thickness of dendrites in each condition ($n \geq 100$), we observed ~15% and ~25% increases in thickness from 10 mM and 50 mM $AuCl_3$ solutions, respectively, while dendritic morphologies were fully preserved (Figure S3B). In contrast, staining with a 100 mM $AuCl_3$ solution resulted in excessive Au nucleation, leading to thicker and heterogeneous morphologies (Figure S3C). Notably, the thickness reached a plateau after 0.5 min across both concentrations, indicating fast reaction kinetics and self-limiting behavior beyond a certain extent (Figure S3D). The thickness increase is attributed to the nucleated Au nanoparticles on the Li surface and possible partial alloying at the interface. These results demonstrate that under optimized staining conditions, the overall dendrite morphology and thickness are well preserved at the individual dendrite level.

Furthermore, we extended the redox staining technique to detect inactive Li^0 at the discharged state, demonstrating its selectivity for Li^0 over SEI species (Figures 1G and S3). In contrast to SEM-EDS analysis on pristine residual SEI at the discharged state (Figure S4A), residual SEI stained after 1 cycle (Figure 1G) and 40 cycles (Figure S4B) exhibited regions of brighter contrast (SEM) with strong Au M signals (EDS), indicating selective visualization of inactive Li^0 particles embedded within residual SEI. Our model experiments with Li_2O, LiF, Li_2CO_3, and PEO NPs, representative of common inorganic and organic SEI species, confirmed that staining is unlikely to occur within the initial few minutes on SEI components (Figure S4C). The selectivity of the technique toward Li^0 originates from its metallic bonding and reductive nature. The redox reaction between solid metal particles and metal ions, driven by their potential difference, is a rapid process commonly utilized in the synthesis of hollow metal nanocrystals known as galvanic replacement reactions.[31] Galvanic replacement reactions between metal ions and solid oxide nanocrystals have been reported but not between highly ionic compounds such as those of alkali metals due to their strong ionic bonds.[32] We believe that the large activation energy for the chemical transformation of Li-based compounds likely shows slow kinetics compared to that of the metallic phase (Li^0), resulting in the selectivity shown from SEM-EDS (Figures 1G and S4A,B). In addition, the SEI in the swollen state enabled dissolved staining precursor ions to diffuse through and react with inactive Li^0.[33] These results are noteworthy because inactive Li^0 could then become chemically and spatially distinguished from the surrounding SEI at the discharged state.

Utilizing Au as a label, we have demonstrated that a selective redox reaction takes place on the surface of Li^0 while preserving the morphology for both active and inactive Li^0. The development of this staining technique is significant and universally applicable to studying Li^0 plating in battery systems. It not only allows for the chemical distinction of Li^0 from other anode components but also enables direct visualization with multiple characterization tools. Below we showcase multiscale applications of the technique, ranging from nanoscale Li dendrites to microscale and even close to the electrode scale using cryo-EM, SEM-EDS, and X-ray computed tomography (XCT), respectively. This integrative approach can provide a more comprehensive view of inactive Li^0 to elucidate its impact on the battery performance.

Validation of the Staining Mechanism Using Cryo-EM and Cryo-ET

We performed cryo-EM on Li dendrites stained with Au to assess the mechanism of redox staining at the nanoscale (Figure 2). The cryo-EM image showed a Li dendrite covered by sub-10 nm NPs of darker contrast, indicating the presence of higher Z elements than Li^0 (Figure 2A, top). The enhanced contrast on the surface allowed the dendrite to stand out from the background in a large field of view (Figure S5A). A high-resolution image with its Fast Fourier Transformation (FFT) displayed lattice spacings (~0.232 nm) that matched well with Au(111) (Figure 2A, the bottom left inset).[27] Additionally, increasing the reaction time to 1 h completely covered the dendrite with NPs, suggesting the redox reaction progressed over time (Figure S5B). Thus, cryo-EM results confirmed that Au^{3+} ions nucleate into Au NPs and remain colocalized on Li^0 as tags and enhanced the contrast under electron beam irradiation.

We employed cryogenic electron tomography (cryo-ET) to visualize the stained dendrite in 3D and demonstrate that Au NPs cover the Li^0 surface in all planes.[34,35] Although cryo-EM can locate NPs, their signals overlap with Li^0 while viewed in projection in a transmitted 2D image. Cryo-ET can visualize the dendrite in 3 dimensions (3D) by collecting a series of 2D images while tilting the TEM stage from −60 to +60° (Figure S5C). A reconstructed 3D volume density of the stained dendrite is shown in Figure 2B and Movie S1. In contrast-

https://doi.org/10.1021/jacs.6c05427
J. Am. Chem. Soc. 2026, 148, 30019−30028

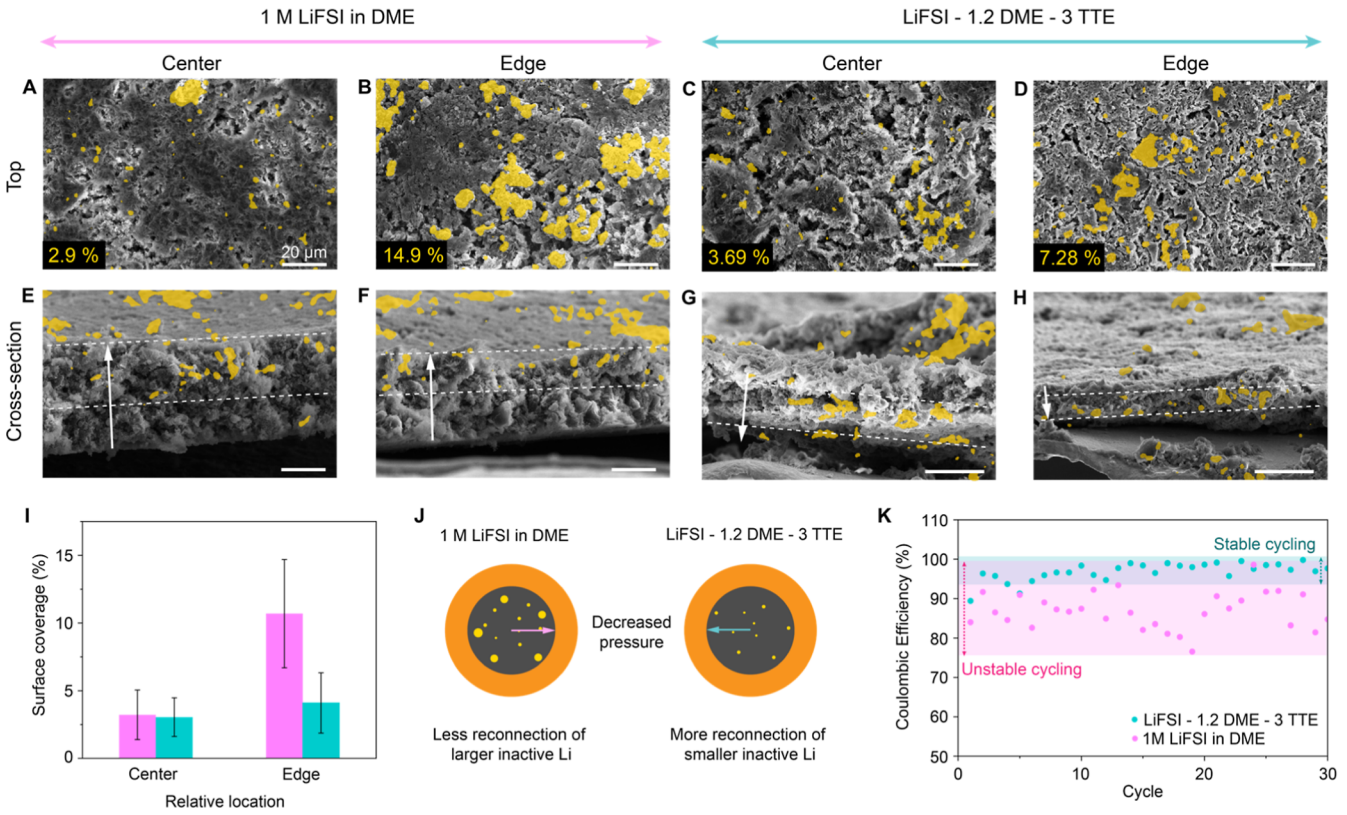

Figure 3. Correlation between the location of inactive $Li^0$and performance. (A–H) Representative SEM images merged with the Au M EDS map (yellow) of stained residual SEI after 30 cycles (1 mA cm^{-2}, 1 mAh cm^{-2}) with 1 M LiFSI in the DME (1 M DME) electrolyte and LiFSI - 1.2 DME −3 TTE (LHCE) electrolyte. Scale bar, 20 μm. (A–D) Top-view images using the 1 M DME electrolyte (at the center (A) and at the edge (B)) and LHCE electrolyte (at the center (C) and at the edge (D)). (E–H) Cross-sectional view images using the 1 M DME electrolyte (at the center (E) and at the edge (F)) and LHCE electrolyte (at the center (G) and at the edge (H)) (Tilt = −10°). (I) Surface coverage of inactive Li^0 over relative location from (A–D). (J) Schematics depicting spatial distributions of stained Li (yellow) in residual SEI (gray) on Cu (orange) cycled with 1 M DME (left) and LHCE (right). (K) Coulombic efficiencies (CE) of 1 M DME (pink) and LHCE electrolyte (cyan) over 30 cycles. Colored boxes and arrows on the plot indicate the respective ranges of CEs in each electrolyte.

based segmentation, the tomogram clearly displayed NPs located on the surface of the stained dendrite (Figure 2C,D). Further analysis with EDS and EELS cross-validated that the NPs and the dendrite were indeed Au and Li, respectively (Figure 2E). These results corroborate that Au and Li were co-located, indicating that EDS analysis on Au can chemically and spatially identify Li^0.

To investigate the time dependence of the technique, we compared the degree of staining at multiple reaction times (Figure 2F). Right after the staining solution was applied (denoted as 0 min), Au NPs were sparsely distributed on the surface of Li dendrites in all electrolytes tested (a carbonate electrolyte (LP40, 1 M $LiPF_6$ in EC/DEC (1:1)), 1 M DME, and a localized high-concentration electrolyte (LHCE, LiFSI-1.2 DME-3 TTE)). Interestingly, smaller Au NPs were dispersed more uniformly, and the surface coverage increased from 13.2% in LP40 to 18.7% in 1 M DME to 69.5% in LHCE, suggesting lower overpotential for diffusion of Au^{3+} through inorganic-rich SEI[36] and potential dependence of staining kinetics according to SEI chemistry. With an increased reaction time of 2 min, we observed that dendrites became nearly fully covered by Au NPs in all electrolytes, and the surface coverage significantly increased to 95.4% (LP40), 93.9% (1 M DME), and 97.2% (LHCE). This result implies that the surface of Li^0 can be covered within a short reaction time (<2 min), and the degree of surface coverage can be controlled by reaction parameters. On the basis of our observations, we propose a redox staining mechanism (Figure 2G). At its pristine state, Li^0 only emits low-energy characteristic X-ray energy upon exposure to beam sources, thus eluding chemical identification. When M^{n+} ions are dissolved in the staining solution, they nucleate as M^0 NPs on the surface of Li^0 through redox reactions and gradually cover the entire surface. This surface layer of high-Z elements is responsible for improved visibility by enhancing contrast and emitting high-energy characteristic X-rays.

We further applied our technique to visualize inactive Li^0 embedded in residual SEI with cryo-STEM (Figure S6). Cryo-STEM images revealed that Li^0 particles could become distinguishable from residual SEI with staining, aligning with SEM-EDS images. On the other hand, it was challenging to identify inactive Li^0 particles within residual SEI using only cryo-STEM with EELS due to the presence of Li atoms in relatively thick SEI from cycling. Zoomed-out images of two different locations of the Cu electrode—the center and the edge—showed that more numbers of individual stained Li^0 particles were visible from the edge. Our results show that the staining technique could be utilized to analyze inactive Li^0 particles from longer cycling with cryo-STEM in the nanoscale.

https://doi.org/10.1021/jacs.6c05427
J. Am. Chem. Soc. 2026, 148, 30019−30028

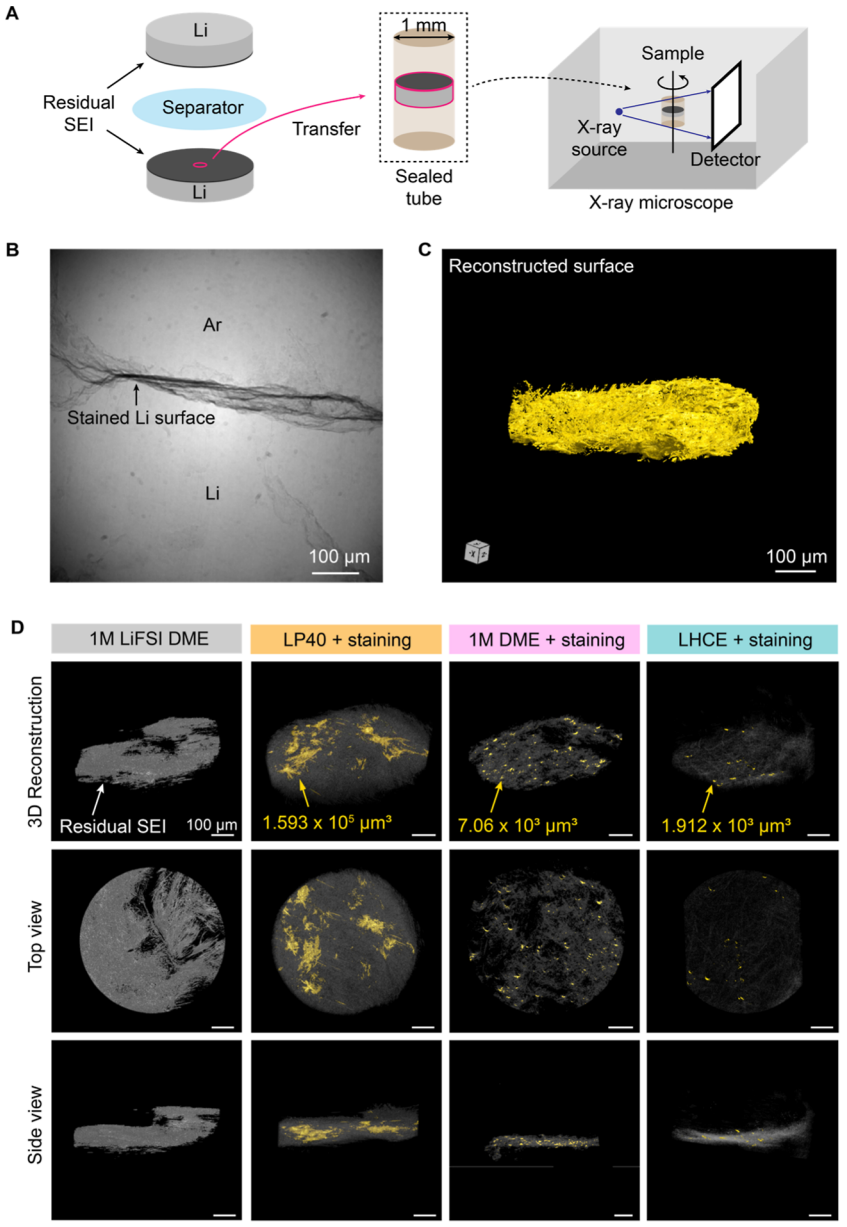

Figure 4. Visualization of Li in residual SEI with X-ray computed tomography (XCT). (A) Schematic illustration on sample preparation for XCT experiments. Center parts of cycled Li^0 were transferred to polyimide tubes (light brown) and sealed to prevent exposure to air. (B) XCT image of surface-stained Li foil. The dark region marked with an arrow represents the stained surface. (C) Reconstructed 3D image of the stained surface from (B). (D) Reconstructed 3D images of residual SEI (gray) after 50 cycles. Reconstructed spatial distribution map of stained inactive Li^0 (yellow) within residual SEI from LP40 (orange), 1 M DME electrolyte (pink), and after staining in LHCE electrolytes (cyan). Scale bar, 100 μm.

Effect of Spatial Distribution of Inactive Li^0 on Battery Performance

At the microscale, SEM-EDS has been widely utilized to observe the morphology of Li^0 in the charged state but not in the discharged state because it is indistinguishable from SEI. A gap exists between cycling factors and their impact on morphology and distribution of inactive Li^0, and their correlation needs to be explored in terms of performance.[2,15,23,37] We utilized the staining technique to reinforce the capabilities of SEM-EDS and image inactive Li^0 from two different ether electrolytes (Figure 3). We focused on the effect of pressure and electrolyte composition as key factors of battery performance in relation to the inactive Li^0 formation. A series of SEM images from the center to the edge of electrodes after staining displayed microparticles with bright contrast corresponding to Au-stained inactive Li^0, as supported by EDS maps of Au M (Figures S7–S9).

Overlaying binary Au M EDS maps onto SEM images enabled 2D spatial mapping of inactive Li^0 as a function of cycling parameters (Figure 3A–H). In both electrolytes, top-view images showed that a larger amount of inactive Li^0 emerged toward the edge, matching our observation from cryo-EM (Figure 3A–D). This trend aligned with previous studies about the dendritic plating of Li^0 near the edge of the electrode, owing to the considerable drop in cell stack pressure.[13,38,39] Cross-sectional images revealed that the staining solution thoroughly wetted residual SEIs and displayed inactive Li^0 near the top surface (Figure 3E–H).[20] However, from at least three replicated samples, the pressure effect was more dominant in 1 M DME electrolyte with a 3.3-

https://doi.org/10.1021/jacs.6c05427
J. Am. Chem. Soc. 2026, 148, 30019–30028

fold increase of surface coverage by inactive Li^0, whereas the increase was only 1.3-fold in LHCE (Figure 3I). The pressure effect was similar in the carbonate electrolyte as well, but it was difficult to make a direct comparison to ether electrolytes from top-view images due to their different plating behaviors (Figure S9). Instead, we observed larger clusters of inactive Li^0 located beneath the top surface of residual SEI. In addition, the average size of Au clusters in 1 M DME (~25.34 μm^2) was about 3-fold larger than in LHCE (~8.76 μm^2). We hypothesized that the inorganic-rich SEI of LHCE induced a thinner residual SEI (~20 μm) with bulkier Li^0 plating morphology than 1 M DME, leading to more homogeneous stripping at the edge, leading to a smaller amount of inactive Li^0 with a smaller size.

On the basis of these results, we propose a correlation between the spatial distribution of inactive Li^0 and cycling behavior (Figure 3J). The majority of inactive Li^0 was visible on the edge parts of the active electrode areas due to a decrease in cell stack pressure, illustrating that decreasing this edge effect could be crucial for mitigating capacity loss. The larger size of inactive Li^0 in 1 M DME is believed to cause significant fluctuation in CE when reconnected (Figure 3K). In contrast, a smaller and lower concentration of inactive Li^0 in LHCE correlates with a higher and more stable CE. Our observations showed how the size and spatial distribution of inactive Li^0 obtained through staining can correlate with cycling parameters. Thus, investigation of spatial and morphological information at a discharged state, which was previously elusive, could contribute to the mitigation of inactive Li^0.

3D Mapping of Inactive Li^0 at the Subelectrode Level

We further visualized inactive Li^0 at a macroscale, in 3D, with XCT to gain 3D electrode-level understanding of inactive Li^0 (Figure 4).[40−43] Although XCT is capable of 3D mapping battery electrodes or solid electrolytes, its application to the Li^0 anode has been limited because most of the X-rays transmit through Li^0. We anticipate stained inactive Li^0 to show significantly darker contrast under X-ray irradiation due to increased Compton scattering of Au and therefore become distinguishable from SEI species at discharged states. Figure 4A depicts the experimental procedure of XCT analysis. After cycling Li||Li cells (1 mAh cm^{-2} at 1 mA cm^{-2}), the electrodes in the discharged state were transferred into polyimide (PI) tubes and sealed under the Ar environment. 2D absorption-based projections of the sample were collected in XCT while rotating 360 deg and merged to reconstruct a volume in 3D.

We first verified the contrast change of Li^0 foil after applying the staining solution onto the surface (Figure 4B,C). Compared to nearly transparent regions corresponding to bulk Li^0, the stained surface exhibited a significantly darker contrast due to the presence of Au (Figure 4B). The surface could be reconstructed based on contrast differences, and the volume well-matched by the XCT images, implying the feasibility of the staining for 3D spatial mapping of inactive Li^0 (Figure 4C and Movie S2).

Residual SEIs of Li||Li cells cycled 50 times in three different electrolytes were used to reconstruct the 3D spatial distribution of inactive Li^0 (Figure 4D). The pristine residual SEI in 1 M DME electrolyte showed a relatively darker contrast against Li^0; however, embedded inactive Li^0 could not be distinguished from the residual SEI without staining (Figures 4D and S10B, Movie S3). XCT images after staining the residual SEI revealed dark spots, which corresponded to Au-stained Li^0, as supported by SEM-EDS (Figure S10C). The reconstruction successfully visualized inactive Li^0 dispersed throughout the residual SEI (Movie S4).

The average size of inactive Li^0 was at a 10 μm-level, and the estimated total volume was 7.06×10^3 μm^3, enabling quantitative analysis in various cycling conditions. In comparison, residual SEI from 1 M $LiPF_6$ in the ethylene carbonate (EC)/diethyl carbonate (DEC) 1:1 (w/w) electrolyte (LP40), a poor electrolyte for LMBs, showed bulkier inactive Li^0 ranging up to 130 μm with a total volume of 1.593×10^6 μm^3 embedded in a thick residual SEI (~100 μm) (Figures 4D and S10D and Movie S5). The estimated total volume of inactive Li^0 decreased to 1.912×10^3 μm^3 with LHCE, a high-performing electrolyte (Movie S6). By converting the volume into Li^0 areal capacity using the relationship

$$(Li^0 areal\ capacity) = \frac{V \times \rho_{Li} \times F}{m_{Li} \times A}$$

inactive capacity remaining in the region of interest was roughly estimated to be 0.12 mAh cm^{-2}, 0.55 μAh cm^{-2}, and 0.15 μAh cm^{-2} for LP40, 1 M DME, and LHCE, respectively (V, ρ_{Li}, F, m_{Li}, and A each stands for total volume of inactive Li^0, density of Li^0, Faraday constant (2.68×10^3mAh mol^{-1}), molecular weight of Li^0, and area of the sample, respectively). The trend in areal capacity was in accordance with the cycling data and accumulative capacity loss in each electrolyte (Figure S10F,G).[2,44] This difference in volume of inactive Li^0 could be explained by the chemistry of SEI. The residual SEI of LP40 is a polymeric framework with unevenly distributed crystalline grains of inorganic species. It is responsible for nonuniform stripping behavior due to variations in spatial ionic conductivity, leading to inactive Li^0 islands that are large in size.[45] Conversely, a significant decrease in the size of inactive Li^0 in 1 M DME could be attributed to its relatively inorganic-rich and homogeneous SEI, followed by a further decrease in LHCE.[20,29] Our results demonstrate that the redox staining technique paired with XCT analysis not only enables 3D visualization but also allows semiquantitative analysis of inactive Li^0 at the subelectrode scale.

We have demonstrated the staining method of Li^0 and its applications for visualization with chemical identification at the multiscale. The key to the selectivity of the technique is that oxidation of Li^0 is the only kinetically favored redox reaction among existing chemicals. Subsequently, the redox staining not only visualizes active Li^0 but also distinguishes inactive Li^0 from SEI at a discharged state. We have demonstrated that our observation on the dependence of inactive Li^0 on electrolytes and relative location from nanoscale (Figure 2) aligns with the trend in microscale (Figure 3), extending to subelectrode scale (Figure 4). The technique enables 3-dimensional spatial and chemical detection of Li^0 simultaneously, with a wide range of detection from the 10 nm-scale to over the 100 μm-scale. In this regard, the conceptual idea of this work can be extended and applied to establish a systematic analysis of active and inactive Li^0 in a broader context. In addition, it is worth noting that the method is relatively simple while being compatible for post-mortem analysis, enabling application to most battery characterizations with minimal modification. This framework is not limited to study Li^0 but could be widely applicable to elements with low electrochemical potential, such as Na or K. Furthermore, we believe that it can be employed to study and

https://doi.org/10.1021/jacs.6c05427
J. Am. Chem. Soc. 2026, 148, 30019−30028

visualize other materials that remain challenging to detect, such as Li dendrite growth in solid electrolytes.

While the Au staining method demonstrated here enables reliable visualization and quantification of metallic Li^0 under the conditions studied, several factors might be of consideration when applying this technique to other systems. First, in cases where the residual SEI is particularly thick, highly passivating, or in a dried state, the diffusion and reaction kinetics of precursor cations might be affected. This may result in a fraction of embedded inactive Li^0 remaining unstained under provided staining conditions, potentially leading to underestimation of total inactive Li^0 content or incomplete spatial mapping. We therefore recommend optimizing staining conditions—including $AuCl_3$ concentration, staining time, and sample preparation protocol—for each specific battery system and considering their potential impacts on the degree of staining. Utilizing model systems of Li^0 at plated and stripped states would be one potential methodology. Second, while the present work demonstrates sufficient $AuCl_3$ penetration through the residual SEI under given staining conditions—as evidenced by successful labeling of inactive Li^0 at the center of residual SEI from XCT results (Figure 4)—a systematic quantification of penetration kinetics as a function of SEI thickness, chemistry, and porosity remains an open challenge. The fast redox reaction kinetics (~30 s saturation), multidirectional diffusion through the three-dimensional SEI matrix at a swollen state, and limited availability of characterization techniques to identify unstained inactive Li^0 make time-resolved penetration analysis difficult with currently available techniques. We identify this as an important direction for future work, which may benefit from in situ or time-resolved characterization approaches.

In this study, we showed that staining Li^0 with heavy elements via selective redox reactions can significantly enhance the contrast of Li^0. The improved contrast was supported by the direct enhancement of visibility of Li^0 in multiscale analysis, from Li^0 dendrites to near-electrode-level investigations. Cryo-EM studies, accompanied by cryo-ET, revealed that Au NPs on the surface of Li contributed to an increased contrast. Furthermore, staining allowed for the spatial location of inactive Li^0 to be visualized by both SEM-EDS and XCT, showcasing the importance of comprehensive analysis of the performance of LMBs. We anticipate that this analytical chemistry technique can lead to further mitigation of inactive Li^0, thus contributing to enhancing the reversibility of the Li batteries.

■ ASSOCIATED CONTENT

Data Availability Statement

All data are available in the main text or the Supporting Information.

Supporting Information

The Supporting Information is available free of charge at https://pubs.acs.org/doi/10.1021/jacs.6c05427.

Additional experimental materials and methods, optical images, SEM-EDS with image analysis, XRD, cryo-EM, XCT, and cycling data (PDF)

3D tomogram of the stained dendrite (AVI)

3D reconstruction of the stained surface (AVI)

3D reconstruction of the residual SEI without staining (AVI)

3D reconstruction of inactive Li^0 dispersed throughout the residual SEI (AVI)

3D reconstruction of bulkier inactive Li^0 embedded in a thick residual SEI from LP40 electrolyte (AVI)

3D reconstruction of inactive Li^0 embedded in a thin residual SEI from LHCE electrolyte (AVI)

■ AUTHOR INFORMATION

Corresponding Authors

Wah Chiu − *Department of Structural Biology, Stanford University, Stanford, California 94305, United States; Division of CryoEM and Bioimaging, SSRL, SLAC National Accelerator Laboratory, Stanford University, Menlo Park, California 94025, United States;* orcid.org/0000-0002-8910-3078; Email: yicui@stanford.edu

Yi Cui − *Department of Materials Science and Engineering, Stanford University, Stanford, California 94305, United States; Stanford Institute for Materials and Energy Sciences, SLAC National Accelerator Laboratory, Menlo Park, California 94025, United States; Department of Energy Science and Engineering, Stanford University, Stanford, California 94305, United States;* orcid.org/0000-0002-6103-6352; Email: wahc@stanford.edu

Authors

Jun Ho Lee − *Department of Materials Science and Engineering, Stanford University, Stanford, California 94305, United States;* orcid.org/0000-0001-8598-7884

Jane K. J. Lee − *Department of Structural Biology, Stanford University, Stanford, California 94305, United States*

Pu Zhang − *Department of Materials Science and Engineering, Stanford University, Stanford, California 94305, United States*

Sarah E. Holmes − *Department of Chemistry, Stanford University, Stanford, California 94305, United States;* orcid.org/0000-0002-7946-964X

Wenbo Zhang − *Department of Materials Science and Engineering, Stanford University, Stanford, California 94305, United States;* orcid.org/0000-0002-0828-594X

Il Rok Choi − *Department of Materials Science and Engineering, Stanford University, Stanford, California 94305, United States; Department of Chemical Engineering, Stanford University, Stanford, California 94305, United States;* orcid.org/0000-0001-5426-2434

Sang Cheol Kim − *Department of Materials Science and Engineering, Stanford University, Stanford, California 94305, United States*

Junyoung Lee − *Department of Materials Science and Engineering, Stanford University, Stanford, California 94305, United States;* orcid.org/0009-0009-9903-2654

Sanzeeda Baig Shuchi − *Department of Chemical Engineering, Stanford University, Stanford, California 94305, United States;* orcid.org/0000-0001-9802-223X

Mun Sek Kim − *Department of Chemical Engineering, Stanford University, Stanford, California 94305, United States*

Zhenan Bao − *Department of Chemical Engineering, Stanford University, Stanford, California 94305, United States;* orcid.org/0000-0002-0972-1715

Complete contact information is available at: https://pubs.acs.org/10.1021/jacs.6c05427

Author Contributions

[▽]J.H.L. and J.K.J.L. contributed equally to the project.

Funding

The funding sources are as follows: Assistant Secretary for Energy Efficiency and Renewable Energy, Office of Vehicle Technologies of the US Department of Energy via the Battery Materials Research (BMR) Program and Battery 500 Consortium (JHL, JKJL, PZ, SEH, WZ, IRC, SCK, JL, SBS, MSK, ZB, YC); CryoEM FWP, Office of Basic Energy Sciences, US Department of Energy, Division of Materials Science and Engineering, DE-AC02-76SF00515. (JKJL, WC); Kwanjeong Educational Foundation through Overseas Graduate Scholarship (JHL, JL); Stanford Energy Postdoctoral Fellowship (SCK); and TomKat Center Graduate Fellowship for Translational Research and Link Foundation Energy Fellowship (SBS).

Notes

The authors declare no competing financial interest.

■ ACKNOWLEDGMENTS

Part of this work was performed at the Stanford Nano Shared Facilities (SNSF) and the Stanford University Cryo-electron Microscopy Center (cEMc). We thank Andrew Barnum and Pinaki Mukherjee for TEM/STEM support at SNSF and Haoqing Wang for help with data collection at cEMC and advice on cryo-ET reconstruction. We thank Michael F. Schmid for the valuable discussion on the manuscript.

■ REFERENCES

(1) Lin, D.; Liu, Y.; Cui, L. Reviving the lithium metal anode for high-energy batteries. *Nat. Nanotechnol.* **2017**, *12*, 194−206.
(2) Fang, C.; et al. Quantifying inactive lithium in lithium metal batteries. *Nature* **2019**, *572*, 511−515.
(3) Tarascon, J.-M.; Armand, M. Issues and challenges facing rechargeable lithium batteries. *Nature* **2001**, *414*, 359−367.
(4) Liu, J.; et al. Pathways for practical high-energy long-cycling lithium metal batteries. *Nat. Energy* **2019**, *4*, 180−186.
(5) Hobold, G. M.; et al. Moving beyond 99.9% Coulombic efficiency for lithium anodes in liquid electrolytes. *Nat. Energy* **2021**, *6*, 951−960.
(6) Xu, W.; et al. Lithium metal anodes for rechargeable batteries. *Energy Environ. Sci.* **2014**, *7*, 513−537.
(7) Chen, K. H.; et al. Dead lithium: Mass transport effects on voltage, capacity, and failure of lithium metal anodes. *J. Mater. Chem. A* **2017**, *5*, 11671−11681.
(8) Weiss, M.; Ruess, R.; Kasnatscheew, J.; Levartovsky, Y.; Levy, N. R.; Minnmann, P.; Stolz, L.; Waldmann, T.; Wohlfahrt-Mehrens, M.; Aurbach, D.; et al. Fast Charging of Lithium-Ion Batteries: A Review of Materials Aspects. *Adv. Energy Mater.* **2021**, *11*, 2101126.
(9) Huang, W.; Ye, Y.; Chen, H.; Vilá, R. A.; Xiang, A.; Wang, H.; Liu, F.; Yu, Z.; Xu, J.; Zhang, Z.; et al. Onboard early detection and mitigation of lithium plating in fast-charging batteries. *Nat. Commun.* **2022**, *13*, 7091.
(10) Zhang, W.; et al. Recovery of isolated lithium through discharged state calendar ageing. *Nature* **2024**, *626*, 306−312.
(11) Liu, F.; et al. Dynamic spatial progression of isolated lithium during battery operations. *Nature* **2021**, *600*, 659−663.
(12) Jin, C.; et al. Rejuvenating dead lithium supply in lithium metal anodes by iodine redox. *Nat. Energy* **2021**, *6*, 378−387.
(13) Fang, C.; et al. Pressure-tailored lithium deposition and dissolution in lithium metal batteries. *Nat. Energy* **2021**, *6*, 987−994.
(14) Xiang, Y.; Tao, M.; Zhong, G.; Liang, Z.; Zheng, G.; Huang, X.; Liu, X.; Jin, Y.; Xu, N.; Armand, M.; et al. Quantitatively Analyzing the Failure Processes of Rechargeable Li Metal Batteries. *Sci. Adv.* **2021**, *7*, 3423.
(15) Tao, M.; et al. Clarifying the Temperature-Dependent Lithium Deposition/Stripping Process and the Evolution of Inactive Li in Lithium Metal Batteries. *ACS Nano* **2023**, *17*, 24104−24114.
(16) Louli, A. J.; et al. Diagnosing and correcting anode-free cell failure via electrolyte and morphological analysis. *Nat. Energy* **2020**, *5*, 693−702.
(17) Niu, C.; et al. High-energy lithium metal pouch cells with limited anode swelling and long stable cycles. *Nat. Energy* **2019**, *4*, 551−559.
(18) Ren, X.; et al. Enabling High-Voltage Lithium-Metal Batteries under Practical Conditions. *Joule* **2019**, *3*, 1662−1676.
(19) Yu, Z.; et al. Rational solvent molecule tuning for high-performance lithium metal battery electrolytes. *Nat. Energy* **2022**, *7*, 94−106.
(20) Wang, H.; et al. Efficient Lithium Metal Cycling over a Wide Range of Pressures from an Anion-Derived Solid-Electrolyte Interphase Framework. *ACS Energy Lett.* **2021**, *6*, 816−825.
(21) Vilá, R. A.; Boyle, D. T.; Dai, A.; Zhang, W.; Sayavong, P.; Ye, Y.; Yang, Y.; Dionne, J. A.; Cui, Y. LiH formation and its impact on Li batteries revealed by cryogenic electron microscopy. *Sci. Adv.* **2023**, *9*, 3609.
(22) Boyle, D. T.; et al. Corrosion of lithium metal anodes during calendar ageing and its microscopic origins. *Nat. Energy* **2021**, *6*, 487−494.
(23) Hobold, G. M.; Gallant, B. M. Quantifying Capacity Loss Mechanisms of Li Metal Anodes beyond Inactive Li0. *ACS Energy Lett.* **2022**, *7*, 3458−3466.
(24) Adrian, M.; Dubochet, J.; Fuller, S. D.; Harris, J. R. Cryo-negative Staining. *Micron* **1998**, *29*, 145−160.
(25) Laporte, M. H.; Klena, N.; Hamel, V.; Guichard, P. Visualizing the native cellular organization by coupling cryofixation with expansion microscopy (Cryo-ExM). *Nat. Methods* **2022**, *19*, 216−222.
(26) de Haan, K.; et al. Deep learning-based transformation of H&E stained tissues into special stains. *Nat. Commun.* **2021**, *12*, 4884.
(27) Yan, K.; Lu, Z.; Lee, H. W.; Xiong, F.; Hsu, P. C.; Li, Y.; Zhao, J.; Chu, S.; Cui, Y. Selective deposition and stable encapsulation of lithium through heterogeneous seeded growth. *Nat. Energy* **2016**, *1*, 16010.
(28) Daniel, M.-C.; Astruc, D. Gold Nanoparticles: Assembly, Supramolecular Chemistry, Quantum-Size-Related Properties, and Applications toward Biology, Catalysis, and Nanotechnology. *Chem. Rev.* **2004**, *104*, 293−346.
(29) Sayavong, P.; et al. Dissolution of the Solid Electrolyte Interphase and Its Effects on Lithium Metal Anode Cyclability. *J. Am. Chem. Soc.* **2023**, *145*, 12342−12350.
(30) Oyakhire, S. T.; Zhang, W.; Shin, A.; Xu, R.; Boyle, D. T.; Yu, Z.; Ye, Y.; Yang, Y.; Raiford, J. A.; Huang, W.; et al. Electrical resistance of the current collector controls lithium morphology. *Nat. Commun.* **2022**, *13*, 3986.
(31) Metraux, G.; et al. Triangular nanoframes made of gold and silver. *Nano Lett.* **2003**, *3*, 519−522.
(32) Oh, M.; et al. Galvanic replacement reactions in metal oxide nanocrystals. *Science* **2013**, *340*, 964−968.
(33) Zhang, Z.; et al. Capturing the swelling of solid-electrolyte interphase in lithium metal batteries - Supplementary. *Science* **2022**, *375*, 66−70.
(34) Nogales, E.; Mahamid, J. Bridging structural and cell biology with cryo-electron microscopy. *Nature* **2024**, *628*, 47−56.
(35) Dai, W.; et al. Visualizing virus assembly intermediates inside marine cyanobacteria. *Nature* **2013**, *502*, 707−710.
(36) Pei, A.; et al. Nanoscale nucleation and growth of electro-deposited lithium metal. *Nano Lett.* **2017**, *17*, 1132−1139.
(37) Xu, S.; Chen, K.-H.; Dasgupta, N. P.; Siegel, J. B.; Stefanopoulou, A. G. Evolution of Dead Lithium Growth in Lithium Metal Batteries: Experimentally Validated Model of the Apparent Capacity Loss. *J. Electrochem. Soc.* **2019**, *166*, A3456−A3463.
(38) Li, Q.; Liu, H.; Wu, F.; Li, L.; Ye, Y.; Chen, R. Recent Advances and Opportunities in Reactivating Inactive Lithium in Batteries. *Angew. Chem., Int. Ed.* **2024**, *136*, No. e202404554.

(39) Wang, M.; Liang, H.; Wang, L.; Zhang, H.; Wang, J.; Wei, Y.; He, X.; Yang, Y. First AIE probe for lithium-metal anodes. *Matter* **2022**, *5*, 3530−3540.
(40) Scharf, J.; et al. Bridging nano- and microscale X-ray tomography for battery research by leveraging artificial intelligence. *Nat. Nanotechnol.* **2022**, *17*, 446−459.
(41) Harry, K. J.; Hallinan, D. T.; Parkinson, D. Y.; MacDowell, A. A.; Balsara, N. P. Detection of subsurface structures underneath dendrites formed on cycled lithium metal electrodes. *Nat. Mater.* **2014**, *13*, 69−73.
(42) Lewis, J. A.; et al. Linking void and interphase evolution to electrochemistry in solid-state batteries using operando X-ray tomography. *Nat. Mater.* **2021**, *20*, 503−510.
(43) Lu, X.; Bertei, A.; Finegan, D. P.; Tan, C.; Daemi, S. R.; Weaving, J. S.; O'Regan, K. B.; Heenan, T. M. M.; Hinds, G.; Kendrick, E.; et al. 3D microstructure design of lithium-ion battery electrodes assisted by X-ray nano-computed tomography and modelling. *Nat. Commun.* **2020**, *11*, 2079.
(44) Liu, H.; Cheng, X.; Xu, R.; Zhang, X.; Yan, C.; Huang, J.; Zhang, Q. Plating/Stripping Behavior of Actual Lithium Metal Anode. *Adv. Energy Mater.* **2019**, *9*, 1902254.
(45) Li, Y.; et al. Correlating Structure and Function of Battery Interphases at Atomic Resolution Using Cryoelectron Microscopy. *Joule* **2018**, *2*, 2167−2177.

https://doi.org/10.1021/jacs.6c05427
J. Am. Chem. Soc. 2026, 148, 30019−30028